A small-scale MRI scanner and complementary imaging method to visualize and quantify xylem embolism formation

Marco Meixner[1,2] (iD), **Martina Tomasella**[3,4] (iD), **Petra Foerst**[1] (iD) and **Carel W. Windt**[2] (iD)

[1]Process Systems Engineering, Technical University of Munich, Gregor-Mendel-Straße 4, 85354 Freising, Germany; [2]IBG-2: Plant Sciences Institute, Forschungszentrum Jülich, Leo-Brandt-Straße 1, 52428 Jülich, Germany; [3]Chair for Ecophysiology of Plants, Technical University Munich, Hans-Carl-von-Carlowitz-Platz 2, 85354 Freising, Germany; [4]Dipartimento di Scienze della Vita, Università di Trieste, Via L. Giorgieri 10, 34127 Trieste, Italy

Summary

- Magnetic resonance imaging (MRI) is a useful tool to image xylem embolism formation in plants. MRI scanners configured to accept intact plants are rare and expensive. Here, we investigate if affordable small-scale, custom-built low-field MRI scanners would suffice for the purpose.
- A small-scale, C-shaped permanent magnet was paired with open, plane parallel imaging gradients. The setup was small enough to fit between leaves or branches and offered open access for plant stems of arbitrary length. To counter the two main drawbacks of the system, low signal to noise and reduced magnetic field homogeneity, a multi-spin echo (MSE) pulse sequence was implemented, allowing efficient signal acquisition and quantitative imaging of water content and T_2 signal relaxation.
- The system was tested visualizing embolism formation in *Fagus sylvatica* during bench dehydration. High-quality images of water content and T_2 were readily obtained, which could be utilized to detect the cavitation of vessels smaller than could be spatially resolved. A multiplication of both map types yielded images in which filled xylem appeared with even greater contrast.
- T_2 imaging with small-scale MRI devices allows straightforward visualization of the spatial and temporal dynamics of embolism formation and the derivation of vulnerability curves.

Introduction

As a result of shifts in temperature and precipitation patterns, forests worldwide are expected to experience an increase in duration and frequency of drought and widespread forest dieback events (Dai, 2013; Park Williams *et al.*, 2013; Trenberth *et al.*, 2014). One of the main causes of drought-induced tree mortality is thought to be embolism formation, resulting in reduced xylem conductivity and, ultimately, hydraulic failure (McDowell *et al.*, 2008; Choat *et al.*, 2018). While there is a good basic understanding of, and a large body of literature on, xylem embolism formation, most of it is based on results obtained by means of invasive methods, applied to excised stem pieces. Only in recent decades have noninvasive imaging methods emerged that allow the spatially explicit visualization of the dynamics of xylem embolism formation and spread (Fukuda *et al.*, 2015).

High-resolution computed tomography (HRCT) is currently the most used noninvasive method and is known for the excellent resolution that it affords (Choat *et al.*, 2016). It has, for instance, been shown to be capable of fully resolving individual xylem vessels in three dimensions (3D; Brodersen *et al.*, 2010, 2011; Choat *et al.*, 2016). However, an important drawback of HRCT is the

use of ionizing radiation. It was found to damage living tissue (Savi *et al.*, 2017) and cause growth inhibition (Dhondt *et al.*, 2010) and disruption of cellular function (Petruzzellis *et al.*, 2018). It is thus less suitable for long-term repeated observations or for investigations of recovery, even though current evidence suggests that xylem vulnerability *per se*, as it primarily depends on the integrity of the dead xylem structure rather than on its living cells and surroundings, is not easily affected by HRCT.

Magnetic resonance imaging (MRI, also known as nuclear magnetic resonance (NMR) imaging) is unusual in that it does not, in contrast to most other imaging or sensing methods, image the absorption of radiation in the visible or X-ray domain. Inside an magnetic resonance (MR) magnet, protons in water within a sample can be excited to emit a weak radio signal. The latter is achieved by means of radio frequency (RF) signals of an appropriate frequency and amplitude, neither damaging nor appreciably heating up the sample. MRI is thus well suited for continuous or long-term measurements. The technology has been used to image structure and anatomy (Robinson *et al.*, 2000; Metzner *et al.*, 2014; Hesse *et al.*, 2018), plant water content (Schepper *et al.*, 2012), and to measure phloem and xylem sap flow (Köckenberger *et al.*, 1997; Scheenen *et al.*, 2000; Windt *et al.*, 2006). For detailed reviews and

more examples see van As *et al.* (2009) and Borisjuk *et al.* (2012). In the scope of plant hydraulics, MRI has been used to study embolism formation (Choat *et al.*, 2010; Fukuda *et al.*, 2015), refilling (Holbrook *et al.*, 2001), hydraulic vulnerability segmentation (Hochberg *et al.*, 2016) and the spread of disease in the xylem (Utsuzawa *et al.*, 2005).

In the context of embolism formation, large high field stationary imagers based on superconducting or resistive magnets have been employed to study grapevine (Holbrook *et al.*, 2001; Choat *et al.*, 2010; Hochberg *et al.*, 2017), woody lianas (Clearwater & Clark, 2003), maple (Zwieniecki *et al.*, 2013) and various herbaceous species (such as the stem of cucumber by Scheenen *et al.* (2007), roots of maize by Ilja Kaufmann *et al.* (2009) and tomato pedicel by van de Wal *et al.* (2017)). However, despite their proven utility, large stationary MRI scanners that are suitable for imaging living plants are rare. The problem is not only the significant cost of such systems, but also the fact that most imagers have an unfavorable hardware configuration. The most limiting factors are: the inaccessibility of the magnet for intact plants (e.g. bore not wide enough, bore horizontal instead of vertical, isocenter not accessible for other reasons); the strength and accessibility of the imaging gradients (imaging gradients do not offer access or cannot be opened, maximum gradient strength too low for microimaging of small samples); or size and accessibility of the RF coil (coil too large relative to the sample to achieve a satisfactory signal-to-noise ratio, coil cannot be split to accept long samples such as stems). For these reasons, imaging plants has so far remained the domain of laboratories that have the technical knowhow to modify their equipment to match the geometry of the plant organ of interest and research question at hand.

Small-scale imagers based on permanent magnets have the potential to make MRI of plants much more affordable and can be tailored for use on plant stems (van As & van Duynhoven, 2013). C-shaped magnets (Umebayashi *et al.*, 2011; Lechthaler *et al.*, 2016) or ring-shaped Halbach magnets that can be opened from the side (Windt & Blümler, 2015) may be especially well suited to image plants. Indeed, a number of such imagers have already been applied to study xylem embolism formation and pine wilt disease (Umebayashi *et al.*, 2011; Fukuda *et al.*, 2015; Ogasa *et al.*, 2016; Umebayashi *et al.*, 2016).

The technology to make small-scale imagers more broadly available thus seems within reach. However, so far, most small-scale MRI scanners still appear to be based on design principles from medical imaging. They employ strong and highly homogeneous magnets, relatively weak imaging gradients, and run single-spin echo (SSE) imaging sequences (i.e. a sequence of commands to operate an MRI scanner; see Fig. 1) with very long echo times. These specifications are optimal for applications on animals or humans, but will have drawbacks for applications on plants. Highly homogeneous magnets have desirable traits: they allow imaging with narrow spectral widths, thus reducing external RF noise; they permit the use of weak imaging gradients, as a result of which gradients can be large and wide, and gradient amplifiers need only modest power; and they allow 3D and multi-slice imaging over large fields of view. However, they will also be wider, heavier and more costly, or have a smaller air gap than is optimal to allow access to plants. Further, their wide but slow

gradients may limit the types of imaging sequences that they can run. SSE has been used by all small-scale MRI studies of plants to date, but in that application it has many drawbacks. Advantageous properties of SSE are that it is robust, does not require fast gradient switching and allows for easy implementation of multi-slice imaging: it is one of the most efficient ways to image a 3D volume with optimal signal to noise. However, in plant stems where 3D imaging is not needed, SSE mainly has drawbacks. In single slice mode it inefficiently samples the available NMR signal (Fig. 1). Furthermore, especially if acquired with long echo times, the resulting images will not only be weighted by water content, but also by tissue-dependent differences in signal relaxation (T_2). SSE images thus do not quantitatively reflect either of these two quantities, and for that reason, may be difficult to interpret.

We propose here that a multi-spin echo sequence (MSE) would be much better suited when imaging plants with small-scale MR imagers, in which field strength inherently limits signal-to-noise performance. Using MSE, the exponentially decaying signal is sampled many times per excitation (Fig. 1). This makes for efficient signal acquisition and enables quantitative proton density imaging, even when long repetition times are required to avoid signal loss as a result of saturation. An additional benefit is that MSE (at short echo times) is relatively insensitive to magnet inhomogeneity (Donker *et al.*, 1997). In
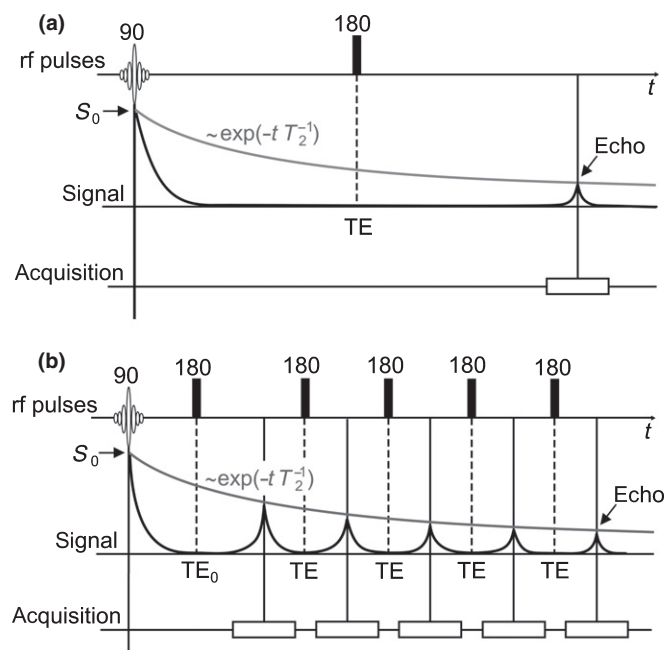

Fig. 1 Comparison of a single-spin echo (SSE) (a) and multi-spin echo (MSE) (b) imaging pulse sequences. In both cases (SSE and MSE) the sample is excited by means of a 90° pulse, after which the signal decays according to the relaxation time T_2, reflecting physicochemical sample characteristics such as proton mobility. In an SSE sequence the signal is refocused by means of a single radio frequency pulse (180° pulse), and acquired after a certain echo time (TE). In the SSE sequence this happens only once and TE is usually chosen to be very long. In the MSE sequence used here, the signal is refocused and acquired many times per excitation and TE is chosen to be as short as possible. S_0 is the amplitude of the signal immediately after excitation.

the data analysis following MSE acquisition, a monoexponential fit of the decaying signal for every pixel in the image will yield quantitative parameter maps of proton density (i.e. water content) and the relaxation time of the signal (T_2). T_2 is highly correlated to water mobility and compartment size (van der Weerd *et al.*, 2000) (also see Theory section). The T_2 relaxation time of water in wide lumina such as xylem vessels is much longer than that in the surrounding tissue, a property that can be measured even if the vessels themselves cannot be resolved (Windt *et al.*, 2007; Schepper *et al.*, 2012; Robert *et al.*, 2014). This may make T_2 a valuable parameter for monitoring the cavitation of vessels, even if they are smaller than the pixels.

In this study we demonstrate how a small-scale MRI scanner and complementary imaging method based on MSE can be used to visualize and quantify embolism formation. We constructed a magnet in which size, weight, robustness, pole gap width and accessibility for stems and branches was prioritized over sheer magnet homogeneity. The device was fitted with custom-built, plane parallel gradients that are open from the front, yet strong and fast enough to enable the use of MSE-type sequences, programmed on a small-scale spectrometer. Embolism formation was visualized and quantified using *Fagus sylvatica* (European beech) as a model species, a tree that is both drought-sensitive and of high economic relevance (Leuschner *et al.*, 2006; Tomasella *et al.*, 2019).

Theory: T_2 relaxation behavior in plants

Nuclear magnetic resonance relies on the fact that certain nuclei have a magnetic moment (spin). In plants the most abundant nucleus with spin is the proton (i.e. the nucleus of hydrogen ^{1}H). When placed in a strong homogeneous magnetic field, protons will orient themselves along with and opposite to the field direction. One of these two states will be slightly more populated, leading to a weak sample magnetization. After exciting the sample with an appropriate RF pulse, a signal can be detected as the protons induce a weak voltage in an RF coil placed around the sample (Schild, 1992; Köckenberger *et al.*, 1997). Two types of signal relaxation can be distinguished: spin-lattice relaxation (T_1) and spin-spin relaxation (T_2) (Haacke *et al.*, 1999). In the context of this study, only T_2 relaxation is of interest.

Spin–spin–relaxation describes the exponential decay of the amplitude of the signal (S) immediately after excitation (S_0), and is strongly correlated with proton mobility (Fig. 1). It reflects intra- and intermolecular proton–proton interactions that cause the signal (S) to decay exponentially as a function of time (t):

$$S = S_0 \exp\left(-\frac{t}{T_2}\right). \qquad \text{Eqn 1}$$

Signal amplitude S_0 thus linearly and quantitatively correlates with proton density, and, after normalizing against a phantom of 100% water, can be used to quantify the amount of water (A) in a pixel in absolute or relative terms.

The T_2 relaxation time of watery solutions in confined compartments or pores is a function of their inherent T_2 relaxation time, and the probability that water molecules of the solution reach the compartment membrane or wall (Brownstein & Tarr, 1979). Protons that pass through membranes are likely to end up in narrow compartments with much smaller relaxation times (cytoplasm, cell wall, intracellular spaces) and thus more rapidly lose their magnetization, or may interact with the compartment wall directly and lose their magnetization in that manner (van As, 2007).

Imaging maize and pearl millet, van der Weerd *et al.* (2001) modeled and demonstrated this correlation in living plant tissue. They modeled T_2 relaxation ($T_{2,\text{obs}}$) as a function of the T_2 of the bulk liquid ($T_{2,\text{bulk}}$) and the surface to volume ratio S/V, the latter of which scales with the inverse of the compartment size:

$$\frac{1}{T_{2,\text{obs}}} = H\frac{S}{V} + \frac{1}{T_{2,\text{bulk}}}. \qquad \text{Eqn 2}$$

The rate of wall relaxation or sink strength density H has been found to vary as a function of membrane permeability (van der Weerd *et al.*, 2000), but differences in compartment size typically dominate T_2. In practice, cells with the largest vacuoles and conduits with the widest diameters give rise to the longest T_2 relaxation times, approximating the T_2 of the bulk liquid (up to 2 s for pure water), whereas narrow pores, conduits or small cells give rise to T_2 values that are much smaller (tens of milliseconds). Correlations between the wide xylem vessels and long T_2 values have been observed in poplar (Windt *et al.*, 2007), cherry (Homan *et al.*, 2007), oak (Schepper *et al.*, 2012) and *Avicennia marina* (Robert *et al.*, 2014).

In this study we test if the correlation between the relaxation time T_2 and compartment size can be utilized to detect water-filled xylem conduits or, conversely, visualize their disappearance as a result of cavitation.

Materials and Methods

Plant material and experimental treatment

Two- to five-year-old European beech (*Fagus sylvatica*) saplings were purchased at a local nursery (Baumschule Veith, Merzenich, Germany) and grown in a glasshouse (16 h : 8 h, 20°C : 16°C, day : night), supplemental lighting provided by a set of metal halogen vapor lamps (SON-T Agro 250 W; Philips Lighting, Eindhoven, the Netherlands). They were watered every second day to capacity.

During the dehydration experiment the plants were continuously illuminated by a sodium vapor lamp (SON-T Agro 400W; Philips Lighting). Three polyethylene reference tubes (inner diameter 1 mm, Perfusor Line; Braun, Melsungen, Germany) were attached to every stem, filled with nickel nitrate-doped water ($T_2 = 66$, 165 and 296 ms). The MRI scanner was mounted around the stems of the intact trees at 110, 110 and 85 cm above the soil, for trees B1, B2 and B3, respectively. Stem diameters at the imaging slice were 10.2, 9.3 and 9.9 mm, respectively; the stem diameters at the base of the tree were 30.6, 22.3 and 34.6 mm. The stems were fixed with aluminum laboratory clamps above and below the position of the MRI magnet, and at the base of the stem. First, MR images of the intact, well-watered trees were acquired. Second, the stems were cut 10 cm above the soil to initiate desiccation. The

distances between the cut end of the stem and the imaging slice were thus 100 cm (B1 and B2) and 75 cm (B3). The drying trees were imaged every 2 h. After the MRI measurements, the imaged stem section was excised and stored at −20°C for microscopy.

MRI hardware and methods

A 0.25 T, 16 kg C-shaped permanent NdFeB magnet with a 35 mm air gap was custom-built and fitted with a three-axis plane parallel gradient set. The gradient set was etched on layers of two-sided 105 μm copper circuit boards (Octamex, London, UK) and mounted on an openable, aluminum frame that also served as a Faraday cage and a heat sink (Fig. 2a). To reduce magnetic field drift resulting from temperature changes, the poles of the magnet were equipped with resistive heating wire and coupled to an accurate temperature controller, regulating magnet temperature to a set point value of 29 °C. The MR imager was connected to a standard Kea II spectrometer (Magritek, Wellington, New Zealand) with a built-in 100 W RF amplifier. The gradients were driven by a set of three BAFPA40 gradient amplifiers (Bruker, Rheinstetten, Germany), yielding a maximum gradient strength of 0.24 T m^{-1} over a spherical volume of 25 mm. Before placing the plant inside the magnet, an 11-turn, 15-mm-diameter solenoidal RF coil was hand-wound around the stem with the help of a split Teflon coil former. The magnet was mounted on an adjustable nonmagnetic stand constructed of aluminum and stainless steel (Fig. 2b). If built in series, it is conceivable that small-scale MR imagers with similar specifications could be produced for less than, for example, a set of high-end portable infrared gas analyzers.

For image acquisition, an MSE (modified Carr, Purcell, Meiboom, Gill sequence (Edzes *et al.*, 1998), with an XY-8 phase cycling scheme) type imaging pulse sequence was used. Imaging was done using the following settings: matrix size 128 × 128, repetition time 1.5 s, 64 echoes, first echo time 3.95 ms, all subsequent echo times 2.01 ms for B1 and 2.1 for B2 and B3. The slice thicknesses were 4.5, 5.5 and 5.0 mm, the fields of view 18.0, 15.5 and 14.7 mm, and the number of averages 32, 32 and 24, for plants B1, B2 and B3, respectively.

All image acquisition and initial data processing were done in PROSPA (Magritek). First, all images were masked and phase corrected according to Ma *et al.* (2008). Quantitative water content (A) and T_2 maps were calculated on the basis of a monoexponential fit of the signal ($S(t)$) for every pixel according to Eqn 1. Water content maps were normalized by dividing them by the average water content value of all three reference tubes. $A \times T_2$ product maps were obtained by performing a pixel-by-pixel multiplication of the amplitude and T_2 maps.

Obtaining vulnerability curves

Before each MR measurement, the plant leaf water potential was determined according to Scholander *et al.* (1964). For this purpose a random twig was bagged, cut off and quickly transferred to a pressure chamber (Model 1000; PMS Instrument Co., Albany, NY, USA). On the basis of calibration curves that were acquired by means of independently obtained dry-down measurements, we found the difference between stem and leaf water potential to be insignificant for beech saplings after stomatal closure occurred, at water potentials of −1.5 MPa and lower.
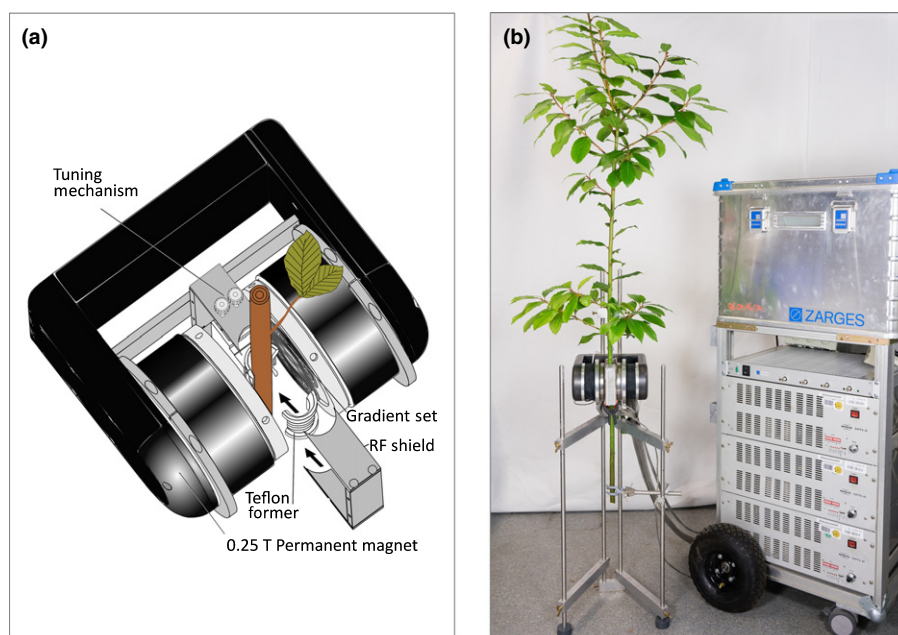

Fig. 2 (a) Schematic representation of the small-scale magnetic resonance imaging (MRI) magnet and plus probe head. The magnet as well as the plane parallel imaging gradient coils are open and fully accessible from the front, allowing trees or branches to be slid in. Arrows indicate how the split coil and the probe head close around the plant. The magnet has an air gap of 35 mm and a spherical homogeneous region of 25 mm in diameter, defining the maximum field of view. The probe head and radio frequency (RF) coil are slightly more restrictive, allowing for a maximum object diameter of 20 mm. (b) The complete instrument. The magnet is borne by an adjustable nonmagnetic support. Three large gradient amplifiers and associated components are mounted in the wheeled aluminum trolley; on top of it an aluminum enclosure is visible that contains the spectrometer.

To obtain vulnerability curves (VCs), xylem masks were created for all measurements. The xylem region was selected by hand, excluding the phloem, bark and reference tubes from further analysis. Slight changes in stem position over the course of the dry-down experiment were corrected by shifting the masks accordingly. VCs were calculated using four different methods. First, by determining the loss of conductivity on the basis of the number pixels lost within binarization masks of (method 1) the amplitude or (method 2) the $A \times T_2$ product maps; and second, on the basis of the loss of the total proton density (i.e. the amount of water per pixel) that was lost during dry-down from within the previously mentioned binarized masks, made on the basis of water content (method 3) or $A \times T_2$ product maps (method 4).

To obtain a relative value for the embolized xylem area (%$_{emb}$), the initial pixel count or amplitude sum ($P_{initial}$) and the final pixel count or amplitude sum (P_{min}) were calculated from the number of pixels above threshold (P_{abv}):

$$\%_{emb} = 100 \times \frac{P_{initial} - P_{abv}}{P_{initial} - P_{min}}. \qquad \text{Eqn 3}$$

The resulting curves of all four approaches mentioned were fitted with a sigmodial function (Pammenter & van der Willigen, 1998):

$$\%_{emb}(\psi_{xylem}) = \frac{100}{1 + \exp\left(\frac{S}{25}\left(\psi_{xylem} - \psi_{50}\right)\right)}, \qquad \text{Eqn 4}$$

where the slope and the position of the curve in x-direction are denoted by S and Ψ_{50}, respectively, the latter indicating the water potential at which 50% of the xylem is embolized. All fits were performed with MATLAB (Mathworks, Natick, MA, USA) and fitting errors were calculated according to Press (2002).

Light microscopy

After the dry-down experiment, the imaged stem pieces were marked and excised. Transverse sections of 20 μm were prepared with a sliding microtome (GSL1; Schenkung Dapples, Zürich, Switzerland) and stained with a 1 : 1 (v/v) mixture of safranin and astrablue, following Gärtner & Schweingruber (2013). Images of the cross-section were obtained with a digital camera connected to a light microscope (Leica Microsystems GmbH, Wetzlar, Germany), at a magnification of ×4 in combination with a digital camera (Kappa PS30; Kappa optronics GmbH, Gleichen, Germany). All images were merged with Adobe PHOTOSHOP CS2 to obtain the picture of the whole cross-section.

Results

Imager and imaging

The half-open C-shaped design of the small-scale MR imager allowed mounting of the setup on a plant in < 20 min. Although still 16 kg, the weight of the magnet was low enough to allow its

position, height and angle to be adjusted easily and by hand. An MSE imaging sequence (Edzes et al., 1998) was implemented and run continuously, which can be thermally challenging for a gradient set without active cooling. Here, up to 64 echoes could be acquired, for all examples shown in this study, without overheating the gradient system. The prototype imager proved to be reliable, allowing continuous operation during several months of tests and dry-down experiments.

Water content and T_2 maps of stems of well-watered beech saplings were acquired, in which seven different types of tissue could be clearly identified (from outside to inside): bark, phloem and cambium, early- and latewood of the annual xylem rings, the pith and (in B1) xylem parenchyma rays. Despite the fact that all trees were furnished by the same grower, were of the same genotype and of comparable heights and stem diameters, their anatomy revealed strongly varying life histories. B1 and B3 had five annual rings at the imaging position, whereas B2 had only two. The current-year annual ring in B1 exhibited evidence of much faster growth than the annual rings from earlier years, whereas both annual rings of B2 showed fast growth.

The most striking features of the parameter maps were the bright bands in the annual rings, which became visible in the amplitude maps as well as in the T_2 maps. The contrast of these bright rings was fairly low in the amplitude maps, but much higher in the T_2 maps and could be improved even more by multiplying the two parameter maps to yield $A \times T_2$ product maps (Fig. 3). The latter procedure resulted in images with excellent contrast and low noise that did not require any image manipulation to remove spikes resulting from erroneous fitting in areas of low signal intensity.

The bright rings of high water content and long T_2 were clearly associated with a high density of wide vessels, except for the oldest annual ring. This was illustrated by matching the microscopic xylem structure accurately with the MR images, overlaying the microscopy image of B3 with its T_2 map (Fig. 4). The water content in those bright rings was c. 70% (Fig. 3, row I), while the darker latewood surrounding those regions showed values of c. 30%. The T_2 maps showed a similar pattern but with much greater contrast (row II). The bright rings had T_2 values of c. 90 ms, while the remaining tissue exhibited values of c. 20 ms. The bright xylem rings in the T_2 maps were slightly wider than those in the amplitude maps.

Imaging embolism formation

During the dry-down experiment three beech saplings were bench dehydrated, while an MR measurement and a water potential measurement were conducted every 2 h. Of the resulting time series of images and water potential measurements, only the five sets that show the most significant changes are displayed (Fig. 5). Videos incorporating all product images that were acquired during dry-down of each plant are provided in Supporting Information Videos S1–S3.

In all parameter maps (water content (A), T_2 and $A \times T_2$) the bright rings in the xylem were found to progressively disappear at increasingly negative water potentials, supporting the idea that
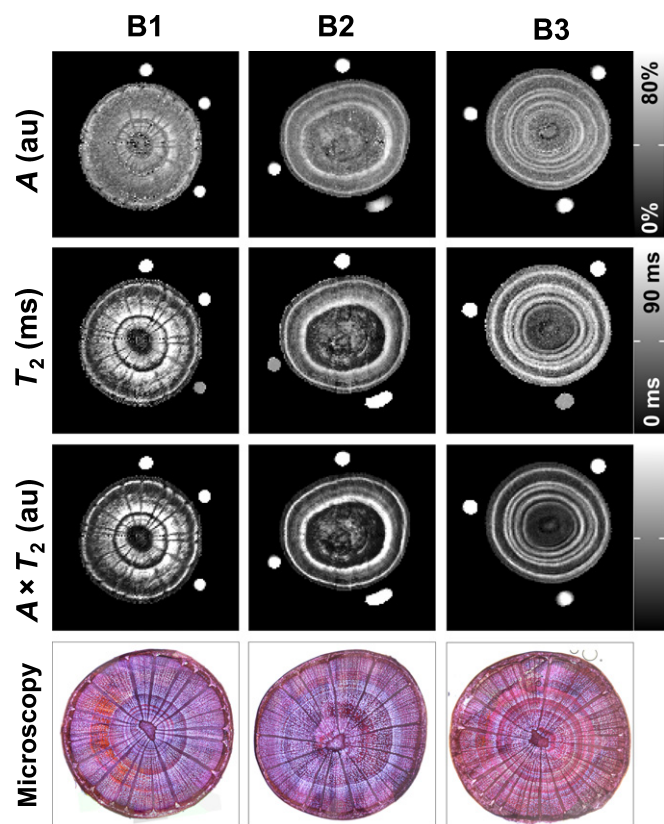
Fig. 3 Comparison of amplitude (A), relaxation time (T_2) and $A \times T_2$ product maps of the stems of three well-watered beech (*Fagus sylvatica*) trees (B1, B2, B3), measured before commencing the dry-down experiment, and optical microscopy of the same positions in the stems after harvesting (bottom row). The first row shows the signal amplitude maps in au, normalized to relate linearly and quantitatively to water content (0–80%); the second row illustrates T_2 relaxation maps in ms; the third shows the product maps of amplitude and relaxation time. Bars indicate the values corresponding with black (minimum) and white (maximum) values. Next to the plants three reference tubes are visible. The fourth row shows microscopy images of each plant at the same position.

Fig. 4 (a) Overlay of the relaxation time (T_2) parameter map and the corresponding light microscopy image of beech (*Fagus sylvatica*) stem B3. Region I of the image shows the T_2 map, region II microscopic image, and region III an overlay of the half transparent microscopy image with the T_2 map superimposed. (b) Magnified view of the region indicated with a dashed box in (a). (c) Further magnification of the region indicated in (b). In this window the grid indicates the magnetic resonance imaging pixel size (120 × 120 μm).

the declining water content and the change in T_2 corresponded with the loss of water from previously filled xylem vessels. The percentage change in water content was much smaller than the percentage change in T_2. The average amplitude loss observed for pixels with filled xylem vessels over the course of the dry-down ranged from 37% to 48% (B1, 37.1%; B2, 48.4%; B3, 35.5%), concomitant with a decrease in water potential of *c.* −1 to < −5 MPa. The corresponding changes in T_2, however, were about twice as large and ranged from 67% to 72% (B1, 72.3%; B2, 71.3%; B3, 67.9%). At the end of the dry-down experiment, at water potentials < −5 MPa, in all three trees the residual xylem water content was *c.* 30% with a T_2 value of around 20 ms. As shown in Fig. 5, the contrast provided by the water content and T_2 maps could be improved even further by multiplying the two parameters. The resulting $A \times T_2$ product maps were found to show even greater percentage changes over the course of the dry-down (B1, 81.7%; B2, 85.0%; B3, 78.9%).

In most beech stems, the oldest annual rings lost water and showed declining T_2 values before the younger ones did. The
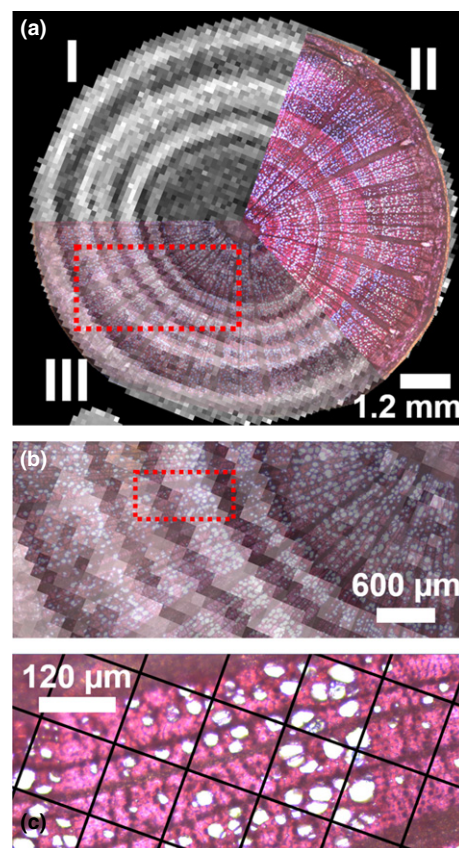
only exception was the second annual ring in B3, which lost water before the third one (rings counted from the outside). For all beech trees, a homogeneous radial spread of emboli within the annual rings was observed, resulting in a narrowing of the bright xylem sections. As the dry-down continued, the radial spread of emboli within the rings was accompanied by a tangential spread. For all trees, the latewood within the rings was affected first (signal decline < −2 MPa), the earlywood last. Before the dry-down, in B1 a domain of low water content and T_2 within the current annual ring was already showing, extending in tangential direction (arrow in Fig. 5a, row III). Below −3 MPa this domain of low water content and T_2 values grew larger and spread in tangential and radial directions.

Vulnerability curves

Four methods to approximate the percentage loss of conductivity (PLC) were tested: (1) calculation of PLC on the basis of the loss of number of pixels containing water-filled vessels, determined on the basis of binarized amplitude maps; (2) as method 1 but calculated on the basis of binarized $A \times T_2$
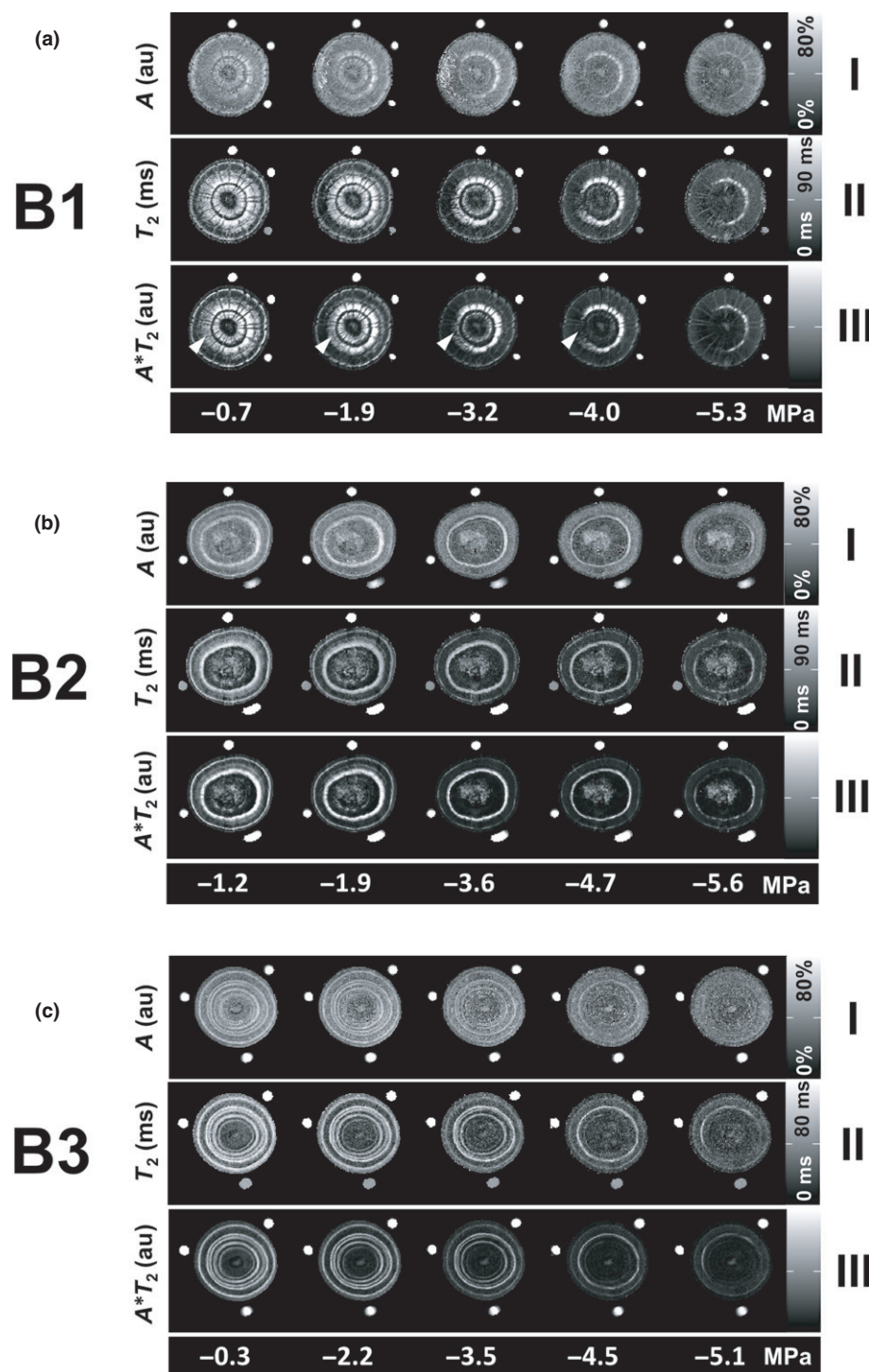
Fig. 5 A comparison of magnetic resonance maps acquired during progressive dry-down of three beech (*Fagus sylvatica*) trees (a–c, B1, B2 and B3, respectively). Row I shows the signal amplitude (*A*), normalized to relate linearly and quantitatively to water content (0–80%); row II shows relaxation time (T_2); row III shows the $A \times T_2$ product maps; corresponding water potential values are shown underneath (WP).

product maps; (3) as method 1 but based on the decrease in the cumulative proton density in the pixels identified by means of binarized amplitude maps; and (4) as method 3 but based on the cumulative proton density in the pixels identified by means of binarized $A \times T_2$ product maps. Masks resulting from the binarization of water content and $A \times T_2$ product maps are shown for five water potential values of B3 in Fig. 6(c,d). Using Eqn 3 and fitting the result with a sigmodial function (Eqn 4), VCs were calculated either on the basis of the number of pixels

in the binarization masks, or by summing up amplitude values of those pixels (Fig. 6a,e,f). The exact values and error values of r^2, slope and Ψ_{50} for each plant are provided in Table S1. All four approaches resulted in VCs that matched the data points well, with values of r^2 close to 1. The vulnerabilities of samples B1 and B3 were found to be very similar (a difference of *c.* 0.1 MPa), whereas the Ψ_{50} of B2 was found to be *c.* 0.6 MPa lower. An additional comparison of the four methods with all plants grouped together, done by means of the FITPLC package
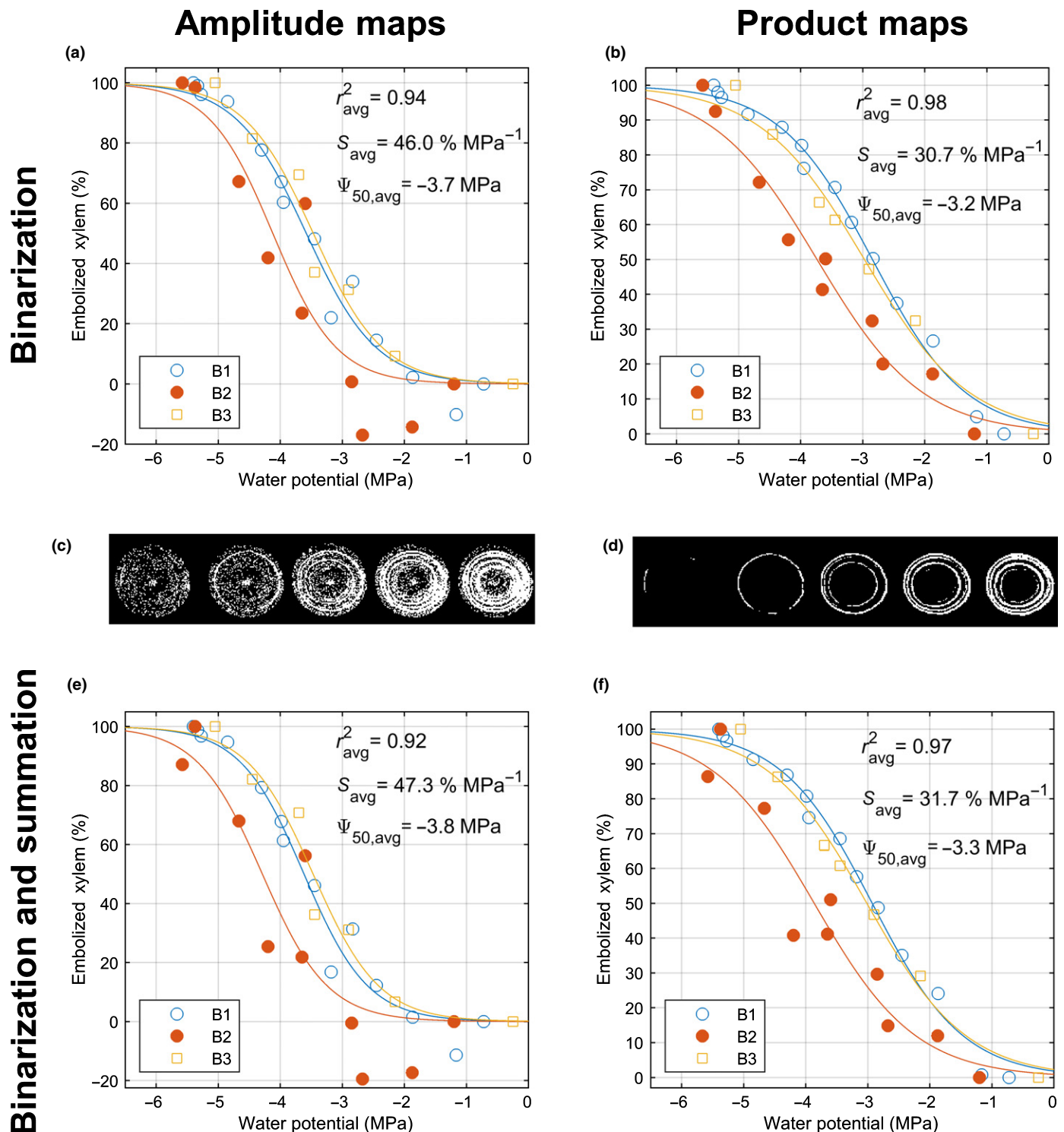
Amplitude maps

Product maps

(a)

$r^2_{avg} = 0.94$

$S_{avg} = 46.0\ \%\ MPa^{-1}$

$\Psi_{50,avg} = -3.7\ MPa$

○ B1
● B2
□ B3

(b)

$r^2_{avg} = 0.98$

$S_{avg} = 30.7\ \%\ MPa^{-1}$

$\Psi_{50,avg} = -3.2\ MPa$

○ B1
● B2
□ B3

(c)

(d)

(e)

$r^2_{avg} = 0.92$

$S_{avg} = 47.3\ \%\ MPa^{-1}$

$\Psi_{50,avg} = -3.8\ MPa$

○ B1
● B2
□ B3

(f)

$r^2_{avg} = 0.97$

$S_{avg} = 31.7\ \%\ MPa^{-1}$

$\Psi_{50,avg} = -3.3\ MPa$

○ B1
● B2
□ B3

Fig. 6 Vulnerability curves (VCs) based on binarized amplitude and amplitude × relaxation time ($A \times T_2$) magnetic resonance images of three beech (*Fagus sylvatica*) trees. (a, b) VCs constructed on the basis of the cumulative pixel area of all pixels with values above a threshold in the amplitude (a) or $A \times T_2$ product images (b). (c, d) Examples of the masks thus created are shown for five water potential values (in MPa: −0.3, −2.2, −3.5, −4.5, −5.1) in B3. (e, f) VCs are shown that were constructed on the basis of the change in water content (i.e. amplitude) inside the same masks as before, made on the basis of amplitude images (e) and $A \times T_2$ product images (f). After normalizing, all curves were fitted with a sigmodial function; in the upper right corner the mean values for r^2, slope S and Ψ_{50} of the curves are shown. For the values of the individual curves see Supporting Information Table S1. For a supplemental analysis of the data with the FITPLC package see Fig. S1.

(Duursma & Choat, 2017), is provided in Fig. S1 and yielded comparable results.

The masks based on the product maps much more clearly reflected the filled xylem than those based on the amplitude maps (Fig. 6c,d). This corresponds to the fact that the contrast between filled and cavitated xylem pixels was much greater in the product maps than in the amplitude maps, as was the signal-to-noise ratio of the respective images.

Compared with VCs obtained from binarized product images (Fig. 6b,f), VCs obtained from binarized amplitude images (a and e) resulted in lower values of r^2, steeper slopes and more negative values for Ψ_{50}.

Discussion

Imaging xylem embolism formation

Despite the low field strength and the relatively low resolution afforded by the small-scale MR imager, our method was remarkably successful at visualizing the appearance and spread of embolism in the xylem. The use of an MSE imaging sequence allowed for efficient signal acquisition, enabling the computation of quantitative water content and T_2 maps. Embolism formation became visible in all three parameter maps that were acquired, water content, T_2 and $A \times T_2$. The multiplication of amplitude and T_2 maps to yield $A \times T_2$ product maps was especially helpful, as it provided even more contrast between filled and empty xylem than did either amplitude or T_2 maps, while also yielding cleaner and less noisy images without any further image processing.

The time resolution of the measurements (2 h) was sufficient to visualize the spread of emboli. Embolism spread happened first radially, from latewood to earlywood (i.e. from outside to inside), and subsequently in a tangential direction. This was indicated by bright (i.e. water-filled) rings becoming narrower from the outer to the inner xylem. We did not observe a spread of emboli between annual rings. This agrees with observations by Fukuda *et al.* (2015), who saw a similar narrowing of rings from outside to inside in Katsura and Japanese birch. Brodersen *et al.* (2013a, b) observed in grapevine a radial spread of emboli as well, but in the other direction, that is, from the pith towards the cambium via direct connections and xylem vessel relays between vessels.

Xylem conduits in the older annual rings of all samples cavitated at less negative water potentials than those in the youngest annual rings. This is in agreement with findings of previous non-invasive studies on angiosperms (Fukuda *et al.*, 2015) and gymnosperms (Umebayashi *et al.*, 2016). The phenomenon has been suggested to be caused by cavitation fatigue, attributed to repeated cycles of drought causing pit membrane degradation (Hacke *et al.*, 2001; Melcher *et al.*, 2003; Hillabrand *et al.*, 2016).

A water content of *c.* 30% remained in the wood after water potentials dropped below −5 MPa, at which point most of the bright rings had already disappeared (Fig. 5). The T_2 value of this remaining water was *c.* 20 ms, which is significantly lower than the T_2 value of regions with filled vessels. The T_2 of the remaining water is depressed, because it resides in narrow lumina such

as fiber tracheids (Schweingruber, 1990). While Fukuda *et al.* (2015), by means of scanning electron microscopy, also found remaining water in fiber tracheids surrounding cavitated vessels in the xylem of Katsura, this water was hardly visible in their MRI images. This may be attributed to the fact they used an SSE imaging sequence with an echo time of 13 ms. After that time, most signal from water in fiber tracheids can be assumed to be lost as a result of T_2 signal relaxation.

Simulating embolism detection by means of T_2 relaxation

Embolism formation in vessels became visible more readily in the T_2 parameter maps than in the water content maps, confirming that T_2 provides a useful parameter with which the presence, and subsequent disappearance, of water in filled vessels with long T_2 relaxation times can be detected amongst the signal of water within the wood around the vessel lumina. The latter pool of water has much shorter relaxation times and is found in narrow structures such as fibers, intracellular spaces, or cell wall matrices. T_2 thus becomes a means to gain subpixel information: if in a pixel sufficient water is present in conduits with a T_2 that is much
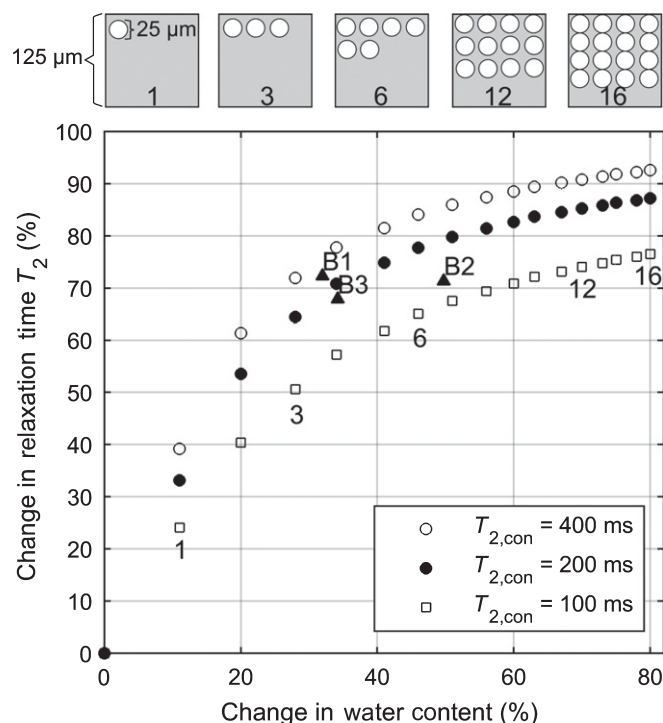

Fig. 7 Modeled relationship of the percentage change in amplitude (*A*) and relaxation time (T_2) that is expected if *n* vessels are present in a pixel, and all cavitate. In the model, pixels had a size of 120 × 120 μm and all conduits had a diameter of 25 μm. The simulation is run for 0–16 conduits with a volumetric water content of 100% with T_2 values of 100, 200 and 400 ms (see key). The wood around the conduits is assumed to have a volumetric water content of 30% with a T_2 of 20 ms. The resulting curves indicate a larger effect on the T_2 value of a pixel than on its amplitude value, in case only a few (one to six) vessels inside of it cavitate. The actual average changes in amplitude and T_2 that were measured in the different beech individuals were added to the graph (filled triangles) and match well with the modeled results.

longer than that of water in the surrounding wood, the T_2 relaxation time of the pixel as a whole will be elevated sufficiently to stand out clearly.

The data acquisition and monoexponential fitting were simulated to compare how the two fit parameters are affected by the presence and subsequent cavitation of varying numbers of vessels inside of a pixel. The NMR signal before cavitation was assumed to be the sum of two pools of water in a pixel: water in conduits (S_{con}), comprising both tracheids and vessels with longer T_2 values ($T_{2,con}$); and water in all other, much narrower spaces in the wood such as fibers and intracellular lumina (S_{other}), with a correspondingly short T_2 ($T_{2,other}$). After cavitation of all conduits in a pixel, the only remaining NMR signal was assumed to originate from water in the wood surrounding the conduit lumina.

The signals of both pools of water were calculated assuming that all space not occupied by conduits was filled by wood, that all conduits had a diameter of 25 μm, and that the water content of the wood before and after cavitation remained at 30%. The conduit diameter was chosen on the basis of the observed conduit diameter distributions (see Fig. S2); the water content of the wood was estimated based on the water content next to the bright rings observed in the water content images. The NMR signal of a pixel was subsequently modeled on the basis of Eqn 1:

$$S_{con} = \frac{n_{con}A_{con}}{A_{pix}} \exp\left(-\frac{t}{T_{2,con}}\right),$$ Eqn 5

and

$$S_{other} = 0.3 \times \left(1 - \frac{n_{con} \times A_{con}}{A_{pix}}\right) \exp\left(-\frac{t}{T_{2,other}}\right),$$ Eqn 6

where n_{con} represents the number of conduits in a pixel, A_{con} their cumulative cross-sectional area, and t the time after excitation. The simulated NMR signal was sampled according to the settings used for the actual image acquisition. The resulting data points were fitted monoexponentially, providing estimates for amplitude and T_2, calculated first for the scenario in which all conduits were filled, second for the scenario in which all were cavitated. To estimate the response of both parameters to cavitation events, the percentage difference between the T_2 values of both scenarios was plotted against their difference in amplitude. The simulation was run for pixels with between 0 and 16 conduits (see pixel sketches in Fig. 7), in which the water in the conduits was modeled to have $T_{2,con}$ values of 100, 200 and 400 ms.

The results of the simulation corresponded well with the percentage change observed in the images (Fig. 7). The curves showed slopes of well over one for between one and five vessels, indicating that the presence and subsequent cavitation of only a few filled vessels already had a large influence on the observed T_2 value of a pixel. Please note that in the model, all vessels within a pixel are assumed to cavitate. For example, the cavitation of a single vessel which covers 3.4% of the pixel area will cause an amplitude change of 11%, but will cause an even larger increase in the T_2 relaxation time of 25–40%, depending on the value chosen for $T_{2,con}$. This difference decreased for larger numbers of vessels.

To facilitate a direct comparison between the parameter maps and the model, the average percentage changes of water content and T_2 within the bright xylem regions were plotted in Fig. 7. In the simulation, between three and seven vessels per pixel (n_{con}) explained the changes that were observed in amplitude and T_2, for a value for $T_{2,con}$ of between 100 and 400 ms. Those values accurately matched the numbers of vessels that have been found per MRI pixel (Fig. 4c).

During dry-down, the bright rings in the T_2 maps that indicate the presence of filled vessels were always equal in width or wider than the bright rings in the amplitude maps. This suggests that, even when in a pixel a few but not all conduits were cavitated, the T_2 value for such a pixel would remain higher. This response would correctly indicate the presence of filled conduits, but be binary in nature, contrary to the amplitude maps, in which the gradual cavitation of conduits in a pixel results in a gradual reduction of intensity. By combining the two parameters by a multiplication into the $A \times T_2$ parameter maps, the strengths of both are combined, boosting contrast and alleviating the problem of the low SNR that is inherent to the use of a low-field MR imager. The near-binary response of T_2 to the presence of filled vessels is also expressed in the width of the bright rings in the xylem. During the course of the dry-down experiment, bright rings were wider in the T_2 maps than in the water content maps. Further, in the final dry-down images (< -5 MPa) the amplitude maps no longer showed evidence of the presence of remaining filled vessels, whereas in the T_2 and $A \times T_2$ maps some pixels with filled conduits still remained (Fig. 5).

The sensitivity of the T_2 relaxation time to the presence of filled vessels is based on the large difference in the T_2 relaxation time of the NMR signal originating from water in wood and conduits. As T_2 increases with conduit diameter, the method is likely to be applicable for all species in which conduit diameters are similar to, or wider than, those of beech. However, to what degree mapping T_2 would yield comparable results in xylem architectures with smaller or fewer vessels than beech remains to be tested. If T_2 in narrow conduits approaches that of water in wood, the T_2 contrast advantage would be lost.

Vulnerability curves

Surprisingly, despite the noisy appearance of the masks resulting from the binarization of amplitude maps (Fig. 6c,d), all four approaches to obtain a measure for the relative loss of conductivity from binarized MR images successfully yielded VCs. The difference in the VCs based on amplitude maps (Fig. 6a,e) is that more water from nonconducting tissues is included. In binarizing the amplitude images much care was taken not to set the threshold too low, which, owing to the high noise floor, could have led to the exclusion of pixels with filled conduits. The application of a conservative threshold, conversely, will have resulted in the inclusion of pixels that contain wood and water, but no filled conduits. The masks based on $A \times T_2$ product maps, thanks to the high contrast and low noise figure of the latter, most effectively singled out pixels with filled conduits.

Vulnerability curves obtained from $A \times T_2$ product masks resulted in curves with a higher r^2, a more shallow slope and a less negative Ψ_{50}, compared with the VCs obtained from the binarized amplitude images. In both cases, the difference between VCs calculated on the basis of the loss of water within the binarized masks (Fig. 7e,f), and those based on the mere number of pixels left in the mask (Fig. 7a,b), was negligible. The most convenient method to derive VCs from the imaging data thus proved the most useful: binarization on the basis of $A \times T_2$ product images, combined with an estimation of the PLC on the basis of the decrease in the numbers of pixels within the binarization masks.

The differences in the estimates of Ψ_{50} for the two methods were relatively minor, ranging from -3.2 and -3.3 ($A \times T_2$ product masks) to -3.7 and -3.8 MPa (amplitude masks). These values are in good agreement with those reported in other studies on beech saplings (Caquet et $al.$ (2009) and Aranda et $al.$ (2015) reported values of -3.0 to -4.0, and -3.0 to -3.7 MPa, respectively), while there are also studies that found less negative values (Cochard et $al.$ (1999) and Barigah et $al.$ 2013) reported values of -2.5 to 3 and -2.5 MPa, respectively). Studies on mature beech trees also resulted in similar values (Lemoine et $al.$, 2002, -2.2 to -3.1 MPa; Herbette et $al.$, 2010, -3.0 MPa; Schuldt et $al.$, 2016, -3.3 to -3.7 MPa; Stojnic et $al.$, 2018, -2.9 to -3.5 MPa; Tomasella et $al.$, 2018, -2.5 MPa). In the framework of the current study we have not been able to cross-correlate our results with established benchmark methods. In future experiments it would be most interesting to follow up on this study by making such a comparison.

Conclusions

In this study we have demonstrated that MRI scanners based on small-scale, low-field permanent magnets are capable of imaging embolism formation in diffuse-porous angiosperms such as beech. By combining such an imager with an MSE imaging sequence, quantitative parameter maps of water content and T_2 signal relaxation could be obtained. While both types of images could be used to detect xylem cavitation, T_2 parameter maps were found to be especially sensitive to it. By multiplying the parameter maps of water content and T_2 relaxation time, $A \times T_2$ product maps could be obtained in which regions with filled vessels could be identified even more clearly. The improved contrast afforded by the $A \times T_2$ product maps also provided a convenient way to obtain VCs by means of straightforward image binarization.

The MSE imaging sequence, as a means to quantitatively map T_2 relaxation times to visualize and detect filled conduits that are too small to be resolved spatially, could also be helpful when used on conventional imagers with much higher field strengths. In such imagers, signal to noise will not be limiting, but T_2 contrast may still be expected to facilitate the detection of filled conduits, if the latter cannot be identified, because of the limited spatial resolution, on the basis of imaging alone.

Author contributions

CWW and MM designed, built and programmed the magnetic resonance imager. MM performed the experiment and analyzed the data. MT prepared the anatomical sections and microscopic images. MM and CWW wrote the manuscript with contributions from PF and MT.

ORCID

Petra Foerst (iD) https://orcid.org/0000-0002-6381-1543
Marco Meixner (iD) https://orcid.org/0000-0002-3992-9920
Martina Tomasella (iD) https://orcid.org/0000-0002-1470-1030
Carel W. Windt (iD) https://orcid.org/0000-0003-2400-5407

References

Aranda I, Cano FJ, Gascó A, Cochard H, Nardini A, Mancha JA, López R, Sánchez-Gómez D. 2015. Variation in photosynthetic performance and hydraulic architecture across European beech (*Fagus sylvatica* L.) populations supports the case for local adaptation to water stress. *Tree Physiology* 35: 34–46.

Barigah TS, Charrier O, Douris M, Bonhomme M, Herbette S, Améglio T, Fichot R, Brignolas F, Cochard H. 2013. Water stress-induced xylem hydraulic failure is a causal factor of tree mortality in beech and poplar. *Annals of Botany* 112: 1431–1437.

Borisjuk L, Rolletschek H, Neuberger T. 2012. Surveying the plant's world by magnetic resonance imaging. *The Plant Journal* 70: 129–146.

Brodersen CR, Choat B, Chatelet DS, Shackel KA, Matthews MA, McElrone AJ. 2013a. Xylem vessel relays contribute to radial connectivity in grapevine stems (*Vitis vinifera* and *V. arizonica*; Vitaceae). *American Journal of Botany* 100: 314–321.

Brodersen CR, Lee EF, Choat B, Jansen S, Phillips RJ, Shackel KA, McElrone AJ, Matthews MA. 2011. Automated analysis of three-dimensional xylem networks using high-resolution computed tomography. *New Phytologist* 191: 1168–1179.

Brodersen CR, McElrone AJ, Choat B, Lee EF, Shackel KA, Matthews MA. 2013b. *In vivo* visualizations of drought-induced embolism spread in *Vitis vinifera*. *Plant Physiology* 161: 1820–1829.

Brodersen CR, McElrone AJ, Choat B, Matthews MA, Shackel KA. 2010. The dynamics of embolism repair in xylem. *In vivo* visualizations using high-resolution computed tomography. *Plant Physiology* 154: 1088–1095.

Brownstein KR, Tarr CE. 1979. Importance of classical diffusion in NMR studies of water in biological cells. *Physical Review A* 19: 2446.

Caquet B, Barigah TS, Cochard H, Montpied P, Collet C, Dreyer E, Epron D. 2009. Hydraulic properties of naturally regenerated beech saplings respond to canopy opening. *Tree Physiology* 29: 1395–1405.

Choat B, Badel E, Burlett R, Delzon S, Cochard H, Jansen S. 2016. Noninvasive measurement of vulnerability to drought-induced embolism by X-ray microtomography. *Plant Physiology* 170: 273–282.

Choat B, Brodribb TJ, Brodersen CR, Duursma RA, López R, Medlyn BE. 2018. Triggers of tree mortality under drought. *Nature* 558: 531–539.

Choat B, Drayton WM, Brodersen C, Matthews MA, Shackel KA, Wada H, McElrone AJ. 2010. Measurement of vulnerability to water stress-induced cavitation in grapevine. A comparison of four techniques applied to a long-vesseled species. *Plant, Cell & Environment* 33: 1502–1512.

Clearwater MJ, Clark CJ. 2003. *In vivo* magnetic resonance imaging of xylem vessel contents in woody lianas. *Plant, Cell & Environment* 26: 1205–1214.

Cochard H, Lemoine D, Dreyer E. 1999. The effects of acclimation to sunlight on the xylem vulnerability to embolism in *Fagus sylvatica* L. *Plant, Cell & Environment* 22: 101–108.

Dai A. 2013. Increasing drought under global warming in observations and models. *Nature Climate Change* 3: 52–58.

de Schepper V, van Dusschoten D, Copini P, Jahnke S, Steppe K. 2012. MRI links stem water content to stem diameter variations in transpiring trees. *Journal of Experimental Botany* 63: 2645–2653.

Dhondt S, Vanhaeren H, van Loo D, Cnudde V, Inzé D. 2010. Plant structure visualization by high-resolution X-ray computed tomography. *Trends in Plant Science* 15: 419–422.

Donker HCW, Van As H, Snijder HJ, Edzes HT. 1997. Quantitative 1H-NMR imaging of water in white button mushrooms (*Agaricus bisporus*). *Magnetic Resonance Imaging* 15: 113–121.

Duursma RA, Choat B. 2017. fitplc. An R package to fit hydraulic vulnerability curves. *Journal of Plant Hydraulics* 4: 002.

Edzes HT, van Dusschoten D, van As H. 1998. Quantitative T_2 imaging of plant tissues by means of multi-echo MRI microscopy. *Magnetic Resonance Imaging* 16: 185–196.

Fukuda K, Kawaguchi D, Aihara T, Ogasa MY, Miki NH, Haishi T, Umebayashi T. 2015. Vulnerability to cavitation differs between current-year and older xylem. Non-destructive observation with a compact magnetic resonance imaging system of two deciduous diffuse-porous species. *Plant, Cell & Environment* 38: 2508–2518.

Gärtner H, Schweingruber FH. 2013. *Microscopic preparation techniques for plant stem analysis*. Remagen, Germany: Verlag Dr. Kessel.

Haacke EM, Brown RW, Thompson MR, Venkatesan R. 1999. *Magnetic resonance imaging: physical principles and sequence design*. New York, NY, USA: Wiley-Liss.

Hacke GU, Stiller V, Sperry JS, Pittermann J, McCulloh KA. 2001. Cavitation fatigue. Embolism and refilling cycles can weaken the cavitation resistance of xylem. *Plant Physiology* 125: 779–789.

Herbette S, Wortemann R, Awad H, Huc R, Cochard H, Barigah TS. 2010. Insights into xylem vulnerability to cavitation in *Fagus sylvatica* L. Phenotypic and environmental sources of variability. *Tree Physiology* 30: 1448–1455.

Hesse L, Leupold J, Speck T, Masselter T. 2018. A qualitative analysis of the bud ontogeny of *Dracaena marginata* using high-resolution magnetic resonance imaging. *Scientific Reports* 8: 9881.

Hillabrand RM, Hacke UG, Lieffers VJ. 2016. Drought-induced xylem pit membrane damage in aspen and balsam poplar. *Plant, Cell & Environment* 39: 2210–2220.

Hochberg U, Albuquerque C, Rachmilevitch S, Cochard H, David-Schwartz R, Brodersen CR, McElrone A, Windt CW. 2016. Grapevine petioles are more sensitive to drought induced embolism than stems. Evidence from *in vivo* MRI and microcomputed tomography observations of hydraulic vulnerability segmentation. *Plant, Cell & Environment* 39: 1886–1894.

Hochberg U, Windt CW, Ponomarenko A, Zhang Y-J, Gersony J, Rockwell FE, Holbrook NM. 2017. Stomatal closure, basal leaf embolism, and shedding protect the hydraulic integrity of grape stems. *Plant Physiology* 174: 764–775.

Holbrook NM, Ahrens ET, Burns MJ, Zwieniecki MA. 2001. *In vivo* observation of cavitation and embolism repair using magnetic resonance imaging. *Plant Physiology* 126: 27–31.

Homan NM, Windt CW, Vergeldt FJ, Gerkema E, Van As H. 2007. 0.7 and 3 T MRI and sap flow in intact trees. Xylem and phloem in action. *Applied Magnetic Resonance* 32: 157–170.

Kaufmann Ilja, Schulze-Till Thomas, Schneider Heike U, Zimmermann Ulrich, Jakob Peter. 2009. Functional repair of embolized vessels in maize roots after temporal drought stress, as demonstrated by magnetic resonance imaging. *New Phytologist* 184: 245–256.

Köckenberger W, Pope JM, Xia Y, Jeffrey KR, Komor E, Callaghan PT. 1997. A non-invasive measurement of phloem and xylem water flow in castor bean seedlings by nuclear magnetic resonance microimaging. *Planta* 201: 53–63.

Lechthaler S, Robert EMR, Tonné N, Prusova A, Gerkema E, van As H, Koedam N, Windt CW. 2016. Rhizophoraceae mangrove saplings use hypocotyl and leaf water storage capacity to cope with soil water salinity changes. *Frontiers in Plant Science* 7: 895.

Lemoine D, Cochard H, Granier A. 2002. Within crown variation in hydraulic architecture in beech (*Fagus sylvatica* L). Evidence for a stomatal control of xylem embolism. *Annals of Forest Science* 59: 19–27.

Leuschner C, Meier IC, Hertel D. 2006. On the niche breadth of *Fagus sylvatica*. Soil nutrient status in 50 Central European beech stands on a broad range of bedrock types. *Annals of Forest Science* 63: 355–368.

Ma J, Slavens Z, Sun W, Bayram E, Estowski L, Hwang K-P, Akao J, Vu AT. 2008. Linear phase-error correction for improved water and fat separation in dual-echo dixon techniques. *Magnetic Resonance in Medicine* 60: 1250–1255.

McDowell N, Pockman WT, Allen CD, Breshears DD, Cobb N, Kolb T, Plaut J, Sperry J, West A, Williams DG et al. 2008. Mechanisms of plant survival and mortality during drought. Why do some plants survive while others succumb to drought? *New Phytologist* 178: 719–739.

Melcher PJ, Zwieniecki MA, Holbrook NM. 2003. Vulnerability of xylem vessels to cavitation in sugar maple. Scaling from individual vessels to whole branches. *Plant physiology* 131: 1775–1780.

Metzner R, van Dusschoten D, Bühler J, Schurr U, Jahnke S. 2014. Belowground plant development measured with magnetic resonance imaging (MRI). Exploiting the potential for non-invasive trait quantification using sugar beet as a proxy. *Frontiers in Plant Science* 5: 469.

Ogasa MY, Utsumi Y, Miki NH, Yazaki K, Fukuda K. 2016. Cutting stems before relaxing xylem tension induces artefacts in *Vitis coignetiae*, as evidenced by magnetic resonance imaging. *Plant, Cell & Environment* 39: 329–337.

Pammenter NW, van der Willigen C. 1998. A mathematical and statistical analysis of the curves illustrating vulnerability of xylem to cavitation. *Tree Physiology* 18: 589–593.

Park Williams A, Allen CD, Macalady AK, Griffin D, Woodhouse CA, Meko DM, Swetnam TW, Rauscher SA, Seager R, Grissino-Mayer HD et al. 2013. Temperature as a potent driver of regional forest drought stress and tree mortality. *Nature Climate Change* 3: 292–297.

Petruzzellis F, Pagliarani C, Savi T, Losso A, Cavalletto S, Tromba G, Dullin C, Bär A, Ganthaler A, Miotto A. 2018. The pitfalls of *in vivo* imaging techniques. Evidence for cellular damage caused by synchrotron X-ray computed micro-tomography. *New Phytologist* 220: 104–110.

Press WH. 2002. *Numerical recipes in C++. The art of scientific computing*. Cambridge, UK: Cambridge University Press.

Robert E, Schmitz N, Copini P, Gerkema E, Vergeldt FJ, Windt CW, Beeckman H, Koedam N, van As H. 2014. Visualization of the stem water content of two genera with secondary phloem produced by successive cambia through Magnetic Resonance Imaging (MRI). *Journal of Plant Hydraulics* 1: e006.

Robinson A, Clark CJ, Clemens J. 2000. Using ^{1}H magnetic resonance imaging and complementary analytical techniques to characterize developmental changes in the *Zantedeschia Spreng*. tuber. *Journal of Experimental Botany* 51: 2009–2020.

Savi T, Miotto A, Petruzzellis F, Losso A, Pacilè S, Tromba G, Mayr S, Nardini A. 2017. Drought-induced embolism in stems of sunflower. A comparison of *in vivo* micro-CT observations and destructive hydraulic measurements. *Plant Physiology and Biochemistry* 120: 24–29.

Scheenen TWJ, van Dusschoten D, de Jager PA, Van As H. 2000. Quantification of water transport in plants with NMR imaging. *Journal of Experimental Botany* 51: 1751–1759.

Scheenen TWJ, Vergeldt FJ, Heemskerk AM, Van As H. 2007. Intact plant magnetic resonance imaging to study dynamics in long-distance sap flow and flow-conducting surface area. *Plant Physiology* 144: 1157–1165.

Schild HH. 1992. *MRI made easy:(–well almost)*. Wayne, NJ, USA: Berlex Laboratories.

Scholander PF, Hammel HT, Hemmingsen EA, Bradstreet ED. 1964. Hydrostatic pressure and osmotic potential in leaves of mangroves and some other plants. *Proceedings of the National Academy of Sciences, USA* 52: 119.

Schuldt B, Knutzen F, Delzon S, Jansen S, Müller-Haubold H, Burlett R, Clough Y, Leuschner C. 2016. How adaptable is the hydraulic system of European beech in the face of climate change-related precipitation reduction? *New Phytologist* 210: 443–458.

Schweingruber FH. 1990. *Anatomy of European woods*. Bern, Switzerland: Verlag Paul Haupt.

Stojnic S, Suchocka M, Benito-Garzón M, Torres-Ruiz JM, Cochard H, Bolte A, Cocozza C, Cvjetkovic B, de Luis M, Martinez-Vilalta J *et al.* 2018. Variation in xylem vulnerability to embolism in European beech from geographically marginal populations. *Tree Physiology* 38: 173–185.

Tomasella M, Beikircher B, Häberle K-H, Hesse B, Kallenbach C, Matyssek R, Mayr S. 2018. Acclimation of branch and leaf hydraulics in adult *Fagus sylvatica* and *Picea abies* in a forest through-fall exclusion experiment. *Tree Physiology* 38: 198–211.

Tomasella M, Nardini A, Hesse BD, Machlet A, Matyssek R, Häberle K-H. 2019. Close to the edge. Effects of repeated severe drought on stem hydraulics and non-structural carbohydrates in European beech saplings. *Tree Physiology* 39: 717–728.

Trenberth KE, Dai A, van der Schrier G, Jones PD, Barichivich J, Briffa KR, Sheffield J. 2014. Global warming and changes in drought. *Nature Climate Change* 4: 17–22.

Umebayashi T, Fukuda K, Haishi T, Sotooka R, Zuhair S, Otsuki K. 2011. The developmental process of xylem embolisms in pine wilt disease monitored by multipoint imaging using compact magnetic resonance imaging. *Plant Physiology* 156: 943–951.

Umebayashi T, Morita T, Utsumi Y, Kusumoto D, Yasuda Y, Haishi T, Fukuda K. 2016. Spatial distribution of xylem embolisms in the stems of *Pinus thunbergii* at the threshold of fatal drought stress. *Tree Physiology* 36: 1210–1218.

Utsuzawa S, Fukuda K, Sakaue D. 2005. Use of magnetic resonance microscopy for the nondestructive observation of xylem cavitation caused by pine wilt disease. *Phytopathology* 95: 737–743.

van As H. 2007. Intact plant MRI for the study of cell water relations, membrane permeability, cell-to-cell and long distance water transport. *Journal of Experimental Botany* 58: 743–756.

van As H, Scheenen T, Vergeldt FJ. 2009. MRI of intact plants. *Photosynthesis Research* 102: 213–222.

van As H, van Duynhoven J. 2013. MRI of plants and foods. *Journal of Magnetic Resonance* 229: 25–34.

van de Wal BAE, Windt CW, Leroux O, Steppe K. 2017. Heat girdling does not affect xylem integrity. An *in vivo* magnetic resonance imaging study in the tomato peduncle. *New Phytologist* 215: 558–568.

van der Weerd L, Claessens MMAE, Ruttink T, Vergeldt FJ, Schaafsma TJ, van As H. 2001. Quantitative NMR microscopy of osmotic stress responses in maize and pearl millet. *Journal of Experimental Botany* 52: 2333–2343.

van der Weerd L, Vergeldt FJ, Adrie de Jager P, van As H. 2000. Evaluation of algorithms for analysis of NMR relaxation decay curves. *Magnetic Resonance Imaging* 18: 1151–1158.

Windt CW, Blümler P. 2015. A portable NMR sensor to measure dynamic changes in the amount of water in living stems or fruit and its potential to measure sap flow. *Tree Physiology* 35: 366–375.

Windt CW, Vergeldt FJ, de Jager PA, van As H. 2006. MRI of long-distance water transport. A comparison of the phloem and xylem flow characteristics and dynamics in poplar, castor bean, tomato and tobacco. *Plant, Cell & Environment* 29: 1715–1729.

Windt CW, Vergeldt FJ, van As H. 2007. Correlated displacement-T_2 MRI by means of a Pulsed Field Gradient-Multi Spin Echo Method. *Journal of Magnetic Resonance* 185: 230–239.

Zwieniecki MA, Melcher PJ, Ahrens ET. 2013. Analysis of spatial and temporal dynamics of xylem refilling in *Acer rubrum* L. using magnetic resonance imaging. *Frontiers in Plant Science* 4: 265.

Supporting Information

Additional Supporting Information may be found online in the Supporting Information section at the end of the article.

Fig. S1 The data points of all three beech trees (*Fagus sylvatica*) were grouped together for analysis, to compare the four methods shown in Fig. 6 by means of FITPLC package (sigmodial model and 1000 resamples).

Fig. S2 Conduit diameter distributions of the microscopic cross-sections of beech (*Fagus sylvatica*) shown in Fig. 1 (the respective mean conduit diameters of B1, B2 and B3 are 28.5, 24.9 and 20.2 μm, respectively).

Table S1 r^2, slopes and Ψ_{50} of vulnerability curves of three beech (*Fagus sylvatica*) trees shown in Fig. 6.

Videos S1–S3 Videos of embolism formation in beech (*Fagus sylvatica*); shown are time series of magnetic resonance product ($A \times T_2$) images of the stem of three beech trees, acquired during progressive dry-down.

Please note: Wiley Blackwell are not responsible for the content or functionality of any Supporting Information supplied by the authors. Any queries (other than missing material) should be directed to the *New Phytologist* Central Office.